J. Hydrol. Hydromech., 73, 2025, 2, 121–131
https://doi.org/10.2478/johh-2025-0008

sciendo Journal of Hydrology and Hydromechanics Institute of Hydrology SAS

A code for the 2D simulation of the steady-state fluid flow in porous blocks containing transmissive fractures

Corrado Fidelibus[1,3*], Chaoshui Xu[2], Zhihe Wang[2], Peter Dowd[2]

[1] Institute of Geosciences and Earth Resources, National Research Council of Italy, Torino, Italy.
[2] School of Chemical Engineering, University of Adelaide, Australia.
[3] Dipartimento di Ingegneria dell'Innovazione, Università del Salento, Lecce, Italy.
[*] Corresponding author. E-mail: corrado.fidelibus@unisalento.it

Abstract: Modelling fluid flow through a porous rock mass containing fractures is a common issue in many applications in civil engineering, mining engineering, and extraction of energy resources such as petroleum, gas, and geothermal heat. Fractures in these applications normally play the dominant role in conducting the fluid through the media but the contribution from the porous rock cannot be ignored, particularly when the relative conductivity is significantly high. In this case, flow through both the fractures and the porous rock must be considered simultaneously and their interactions could potentially be very complex. The Dual Porosity/Permeability Model (DPM) is commonly used to address the problem, however it has in general the limitation of over-simplified representation of fractures and fracture network within the rock mass. In this paper, for the solution of the fluid flow in such media, a numerical modelling approach based on the application of the Boundary Element Method (BEM) on the fluid flow in the block in combination with the Finite Element Method (FEM) on the fractures is presented, where fractures are represented explicitly in the model as discretised boundaries. A code dedicated to this approach was developed and is presented in this paper, together with results from illustrative examples demonstrating the effectiveness of the approach. The proposed method has the additional benefit of reducing computational costs, which is particularly useful for cases with large-scale fracture networks embedded in a conductive rock matrix. The source code is available for downloading at the link: https://github.com/cx-adelaide/BEMFEM_FlowSim.

Keywords: Flow in fractured porous rocks; Flow through fracture networks; Boundary element method; Coupling BEM and FEM solutions; Handling flow discontinuities; Equivalent porous medium.

1 INTRODUCTION

In many applications in civil, mining, petroleum, and environmental engineering, practitioners have to deal with solutions of the fluid flow, contaminant transport and heat transfer in rock masses below the surface. In general, a rock mass contains intact rock and defects at different scales. Defects in this case refer to structural or geometrical discontinuities within the rock mass ranging from micro fissures between mineral grains to fractures at the engineering scale and geological faults at the large scale. The fluid conductivity of these defects is normally several magnitudes higher compared with that of the intact rock and therefore they play a very important role in the solutions mentioned above. The rock matrix contains interconnected pores and therefore it can also conduct fluid flow through the media (Nieber and Sidle, 2010). This ability to conduct the flow (conductivity) is represented by the matrix permeability value which can range from micro- or even nano-Darcy (e.g., fresh granite) to Darcy scales (e.g., sandstones) (Bear and Cheng, 2010). However, in addition to the matrix conductivity, it is of paramount importance to first understand the geometrical/hydraulic features of the network of fissures/fractures within the rock mass.

The fracture networks are usually discontinuous and exhibit spatial variability, presenting significant challenges in a variety of subsurface engineering applications (Neuman, 2005; Kang et al., 2015). In most cases, elongated features commonly form pathways that dominantly facilitate fluid movement through the rock mass (Renshaw, 1999). However, this prevalence complicates the determination of hydraulic properties across different scales (de Dreuzy et al., 2001). The approach of Discrete Fracture Networks (DFNs) offers an appealing method for capturing the complexity of these networks, integrating both deterministic and statistical data available (Cacas et al., 1990; Reeves et al., 2014). Since the foundational works undertaken several decades ago (e.g., Dershowitz and Einstein, 1988) on the conceptualisation and development of these models, DFNs have gained widespread acceptance as valuable tools for estimating the hydraulic and hydro-mechanical responses of fractured rock systems, particularly when direct field experiments are limited by accessibility or scale. They are also particularly useful when artificial networks of connected fractures are used for the simulation of hydraulic behaviours (Huang et al., 2017; Ren et al., 2017; Pan et al., 2010). In addition, DFNs have been extensively utilised in sensitivity analyses to explore the effects on fluid flow from the orientation, size and intensity of fractures (Benke and Painter, 2003; Hyman et al., 2019).

Parameters for generating a DFN can be inferred by monitoring induced seismic events (Bruel, 2007; Xu et al., 2013; Xu and Dowd, 2014) or by integrating direct outcrop and borehole observations (Xu et al., 2020), supplemented by relative probability distributions. In such models, each fracture can be explicitly represented as an elliptical disk or polygonal plane, resulting in an assembly of interconnected elements that closely mirrors the real fracture network. Consequently, DFNs preserve the heterogeneity and anisotropy that are often characteristic and essential for accurate simulation models. When correctly implemented, DFN simulations can effectively constrain the range of likely flow responses observed in field settings (Karra et al., 2015; Pham et al., 2021).

For such a complex system, different simplifications can be made to improve the efficiency of the model depending on the application. If the flow through the rock matrix (e.g., granite) is negligible compared with that through fractures, such as in the case of hot dry rock enhanced geothermal systems, the model can be simplified to only considering the flow through the DFN, by considering all the fractures explicitly, see e.g., Shapiro and Andersson (1985), Cacas et al. (1990), Therrien and Sudicky (1996), Dershowitz and Fidelibus (1999), Pichot et al. (2012) and Xu et al. (2014). However, when the rock mass is highly fractured, explicitly representing all fractures in the simulation is not practicable and the only efficient approach is to use an Equivalent Porous Medium (EPM, see Long et al., 1982).

As for general cases, contributions from the rock matrix have to be considered together with those from the DFN to produce a more realistic flow model. The Dual Porosity/permeability Model (DPM) is commonly used to solve the model: matrix and fractures are treated as two overlapping continuous media with their own hydraulic parameters and a fluid exchange term used to consider the interaction between the two media (Pruess and Narasimhan, 1985). In the original idealised model of Barenblatt et al. (1960), the matrix acts essentially as a source or sink to the fracture network, which is the primary conduit for fluid flow. In this approach, the fracture network is grossly simplified to derive the parameters of the equivalent continuum representing the fractures (Samardzioska and Popov, 2005). The information of fracture network connectivity is normally not correctly preserved in this over-simplification. For this reason, the DPM may be enhanced by embedding a DFN into the rock matrix, leading to the so-called Discrete Fracture-Matrix (DFM) models (Martin et al., 2005; Reichenberger et al., 2006; Sandve et al., 2012), implemented in commercial codes such as COMSOL Multiphysics® (COMSOL AB, 2024). In such models, only one mesh (or grid) is used for both fractures and matrix. However, when conforming meshes are used, the generation is challenging (Březina and Stebel, 2016). Elongated elements are produced consequently due to the complicated geometry of DFNs, therefore the approach seems more applicable when relatively few (and persistent) fractures dominate the fluid flow. Such difficulties can be circumvented if numerical methods other than the Finite Element Method (FEM) or Finite Difference Method (FDM) are used, such as the Boundary Element Method (BEM), or more recently, the Virtual Element Method (VEM, see Berrone et al., 2018). In essence, with BEM or VEM methods, the mesh/grid generation of the matrix in between the fractures is no longer necessary. In the work described below, the more conventional BEM is considered.

Several contributions concern the application of BEM to fluid flow solutions in rock masses. Shapiro and Andersson (1983) proposed a combination of a discrete fracture network and a continuum-like medium. In the near-field, the steady-state fluid response was formulated by using BEM for the porous matrix and one-dimensional equations for the fractures were explicitly introduced. In the far-field, for the continuum conceptualisation, a semi-analytic technique, based on the discretisation of Green's third identity, was applied. Elsworth (1986) introduced super-elements for a 3D network of fractures with an impervious matrix. In this approach, one such element was used for each fracture of the network, the model was built by resorting to a BEM discretisation covering only the fracture edges and internal intersections, and the resulting set of equations were manipulated by using a standard FEM technique. Rasmussen et al. (1989) solved the fluid flow in each fracture by using a 2D BEM scheme with discretisation of both fracture edges and linear intersections with other fractures, where the fluid flow in the matrix blocks was defined by resorting to a 3D BEM scheme. In their approach, the fractures constitute a system separate from the matrix, therefore the fluid flow from fractures to the matrix was disregarded. Lough et al. (1998) and Lee et al. (2001) further improved the solution of Rasmussen et al. (1989) and extended it to medium-sized or even larger fractures using a BEM scheme. Later, Lenti and Fidelibus (2003) proposed an advanced BEM technique in which quadratic elements were used for fracture edges and constant elements for internal intersections. Constant BEM elements were used due to the need for an agile handling of the flux discontinuities at the intersections between traces of intersecting fractures and between a trace and an edge of a fracture. Yang et al. (2016) and Chen et al. (2018) proposed a BEM approach to model transient shale gas flow problem in a 2D infinite domain where BEM with constant elements was used to solve matrix flow, whereas finite differences were used to solve 1D fracture flow, all combined to a Laplace transform to resolve the transient flow. Xu et al. (2018) used BEM for the simulation of a steady-state fluid flow system in 3D fracture networks in the framework of an iterative solution process, where the flows in all fractures are separately defined and adjusted through iterations to better represent the reality of the flow regime. Finally, Wang et al. (2022) used discontinuous quadratic elements, in conjunction with a parallel Domain Decomposition Method (DDM), to simulate the steady-state fluid flow in 3D fracture networks.

As demonstrated in Dershowitz and Fidelibus (1999), BEM has many clear advantages in terms of efficiency, accuracy, and numerical stability when dealing with the simulation of steady-state fluid flow in fracture networks. Specifically, the discretisation is limited to the outer and inner (the fractures) boundaries, thus the pre-processing is agile with no special prescriptions, and elements of equal size for each fracture and each outer boundary can be assumed. In fact, the intersections among fractures, even when the angles are small, are easily handled without leading to large imprecision. In addition, if constant elements are used, the flux discontinuities at the intersections are (artificially) avoided. It is worth noting that the fracture network in a rock mass is normally stochastically generated, so it is convenient to adopt a solution providing only the relevant quantities (i.e. the fluxes at the edges), given that multiple generations may be requested to define the statistics of the final solution.

In this paper, an approach based on the use of BEM in conjunction with FEM to solve the fluid flow in a porous rock with conductive fractures is proposed (BEM/FEM approach). In this approach, fractures and fracture networks within the rock mass are represented explicitly in the model and therefore fracture topology and fracture network connectivity are fully preserved. BEM is used to numerically solve the Laplace equation for the fluid flow in the porous material, whereas the fluid flow in the fractures is handled through a FEM representation; the FEM equations are coupled with the BEM system by including terms representing the fluid exchange between the two media. Both porous material and the fractures are included in the BEM solution system. It has been demonstrated herein that with the proposed approach, the solution of even reasonably articulated DFNs is acceptable in terms of accuracy with relatively few nodes/elements, so as to obtain an important reduction in both the meshing work and the computational demand. However, the solution for large DFNs with hundreds of thousands of fractures would be still impracticable, and therefore it is suggested that the approach is better used for sub-domains in applications such as the quantification of the single-porosity equivalent (or effective) conductivity of a fractured porous rock mass. The content of the paper mainly refers to this specific issue.

It is worthwhile to note that the application of the proposed approach could be extended to the solution of the steady-state fluid flow with diverse boundary conditions or even to the solution of more articulated models, such as the partially-saturated fluid flow with a net air-water interface (Rasmussen, 1991), or the partially saturated poroelastic medium (Li and Schanz, 2013), provided that the fundamental solution of the specific problem is found (see section Theory). The proposed method described herein is implemented in a code available at https://github.com/cx-adelaide/BEMFEM_FlowSim.

The content of the paper is as follows: in section Theory, the equations for the 2D steady-state fluid flow problem in a porous block with fractures are described; in section Numerical solution, the numerical derivations to solve the system of equations are presented; some validation examples are then given in section Numerical validations; a simple application of the approach is illustrated in section Application example; and finally, concluding remarks are provided in the last section.

2 THEORY

In what follows, with reference to a two-dimensional scheme and an x,y system of coordinates, the equations governing the steady-state fluid flow in the porous medium and the fractures of a rock mass are reported separately.

2.1 Porous medium

The fluid flow in the porous medium, coinciding with the rock matrix, assumed homogeneous and isotropic, is ruled by the Darcy's law:

$$\mathrm{q} = -K\mathrm{grad}h \tag{1}$$

where q is the specific discharge (ms^{-1}), K is the (rock matrix) hydraulic conductivity (ms^{-1}), and h is the hydraulic head (m).

For the steady-state fluid flow, the Laplace equation holds:

$$\nabla^2 h = 0 \tag{2}$$

defined in a domain Ω, coincident with the porous medium, and contoured by Γ.

2.2 Fractures

As far as the fractures are concerned, a conventional idealisation is to assimilate fractures to a rectangular void of no width, in other words, the long sides (the fracture walls) of each rectangle coincide and the fracture degenerates into a *slit*. With reference to Figure 1, for a given not-connected fracture, by assuming a local coordinate ξ, η (ξ along the slit from the first extremity to the second extremity, and η direction according to the right-handed rule, in m) the fracture discharge Q(ξ) (m^{2}s^{-1}) can be functionally related to h(ξ) as follows:

$$Q = -T\frac{\mathrm{d}h}{\mathrm{d}\xi} \tag{3}$$

where T is the fracture transmissivity (m^{2}s^{-1}).

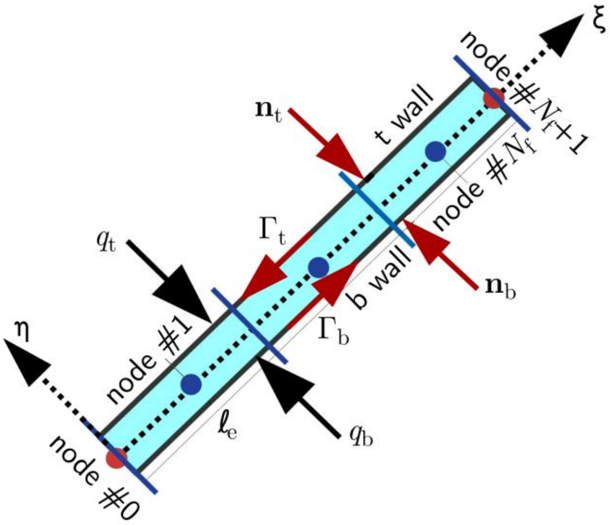

Fig. 1. Isolated fracture as a slit: Γ_b and Γ_t - top (t) and bottom (b) boundaries of the fracture; n_b and n_t -corresponding normal; q_b and q_t - normal component of the specific discharge entering the fracture from b wall and t wall, respectively; nodes (blue dots) of the discretisation, auxiliary nodes at the extremities for the evaluation of the discharge (red dots).

The top (t) wall (positive η) and the bottom (b) wall (negative η) of the slit coincide, however, for the numerical solution proposed herein, they are considered formally separate boundaries Γ_t and Γ_b, with outward normals n_t and n_b, and contouring a void of zero area. The compound perimeter is $\Gamma_\mathrm{f} = \Gamma_\mathrm{t} \cap \Gamma_\mathrm{b}$. The quantities q_t and q_b are also introduced, corresponding to the normal components of the specific discharge q at the t wall and at the b wall, positive if it "feeds" the fracture (i.e., a fluid source to the fracture), constituting the exchange between the fracture and the matrix.

The continuity equation for the fracture is:

$$\frac{\mathrm{d}Q}{\mathrm{d}\xi} - q_\mathrm{t} - q_\mathrm{b} = 0 \tag{4}$$

with ξ local coordinate, such that $0 \leq \xi \leq \ell$, being ℓ the fracture length. By inserting Equations 3 and 4 one has:

$$T\frac{\mathrm{d}^2 h}{\mathrm{d}\xi^2} + q_\mathrm{t} + q_\mathrm{b} = 0 \tag{5}$$

The quantity q_f, equal to the sum of q_t and q_b, can be introduced; it represents the net discharge entering the fracture. Connected fractures in a network are subdivided into *branches*, i.e., segments of fractures between two intersections with other fractures or between an intersection with another fracture and the external boundary.

The continuity equation at an intersection I is:

$$\sum_{i=1}^{n_\mathrm{ib}(I)} Q_i = 0 \tag{6}$$

where Q_i is the discharge of the fracture branch i and $n_\mathrm{ib}(I)$ the number of intersecting branches in I.

For an unconnected extremity of a branch (or of an isolated fracture), the condition of the extremity is $Q(\xi=0)=0$, or $Q(\xi=\ell)=0$, ℓ being this time the length of the branch.

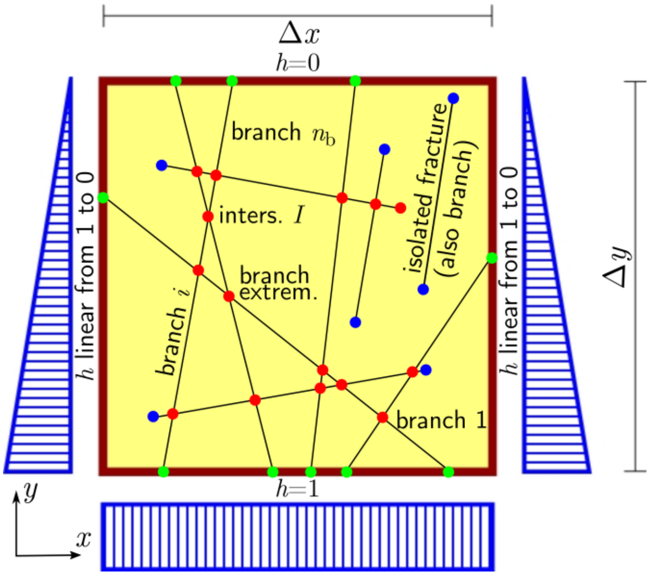

Fig. 2. A rectangular block of a porous medium with discrete fractures subjected to a directional hydraulic gradient: green nodes - intersections among fractures and block boundary, fixed hydraulic head h; blue nodes - unconnected fracture extremities, fracture discharge Q equal 0; red nodes - intersections among fractures, Equation 6 holds; n_b - number of branches.

2.3 Boundary conditions

The quantification of the equivalent (or effective) conductivity of a porous block of size Δx, Δy with inner fractures can be conducted following a method proposed by Priest (1993) and later perfected by Ronayne and Gorelick (2006), consisting of the application of directional hydraulic gradients J_{y+}, J_{y-}, J_{x+}, J_{x-}, induced by specific boundary conditions at the boundaries of the block and the computation of the total discharges at the edges of the block. For example, with reference to Figure 2, to apply the directional gradient along y^+, the following Dirichlet conditions are applied: h=1 on the bottom edge (y=0), h=0 on the top edge (y=Δy), and a linear distribution from 1 to 0 on both vertical edges. Consequently, the imposed directional hydraulic gradient $J_{y+}=-|\text{grad}h|$ is equal to $(1/\Delta y)$.

For a fracture intersecting a boundary, the imposed hydraulic head at its extremity is the one imposed on the intersected boundary at the location of the intersection.

2.4 Numerical solution

A new approach is proposed herein to numerically solve Equations 2, 5 and 6, with reference to a rectangular domain of a porous media with an embedded fracture network subjected to the boundary conditions described in the previous section. The approach consists of the application of BEM for Equation 2 and FEM for Equation 5. The equations are coupled via the exchange of fluid flow quantities between the porous medium and fractures. In what follows the numerical development of both the equations is described.

The Boundary Element Method (BEM) formulation, used herein to numerically transform Equation 2, is derived from the application of the Green's theorem for h and for an auxiliary function h^* linked to h (Brebbia and Dominguez, 1992):

$$\int_\Omega (h\nabla^2 h^* - h^*\nabla^2 h)\mathrm{d}\Omega = \int_\Gamma \left(h\frac{\mathrm{d}h^*}{\mathrm{d}n} - h^*\frac{\mathrm{d}h}{\mathrm{d}n}\right)\mathrm{d}\Gamma \tag{7}$$

where, with reference to the scheme previously introduced, Ω coincides with the rectangular block of porous medium and Γ is composed by the block perimeter Γ_e and the compound of the boundaries $\Gamma_f(i)$ of the n_b fracture branches in the rectangular block (Figure 2). Note that in what follows also the isolated fractures are included in the set of n_b branches. The auxiliary function h^* is the solution of the fundamental Laplace equation:

$$\nabla^2 h + \Delta(P, P^*) = 0 \tag{8}$$

where $\Delta(P,P^*)$ is the Dirac function, defined in all $P(x,y)$ in Ω and for a collocation point $P^*(x^*,y^*)$, and equal to zero everywhere except in P^*, where it tends to infinity. The solution of Equation (8) in two dimensions is:

$$h^*(P, P^*) = \frac{1}{2\pi}\ln\frac{1}{r(P,P^*)} \tag{9}$$

where $r(P,P^*)$ is the geodetic distance between P and P^*. Given the property of the Dirac function and Equation 2, the left hand side integral in Equation (7) is equal to $-h(P^*)$, thus Equation (7) can be arranged as follows:

$$c(P^*)h(P^*) + \int_\Gamma h\frac{\partial h^*}{\partial n}\mathrm{d}\Gamma = \int_\Gamma h^*\frac{\partial h}{\partial n}\mathrm{d}\Gamma \tag{10}$$

where $c(P^*)$ is a coefficient equal to 1 when the collocation point P^* is in Ω, whereas, when P^* is in Γ, it is dependent on the shape of the boundary; in particular, when the boundary is smooth, $c(P^*)$ is equal to 1/2. Equation 10 is the base equation of the BEM formulation. Note that the equation involves boundary quantities only, provided that the collocation point is in Γ. Equation 10 can be re-written as follows:

$$c(P^*)h(P^*) + \int_{\Gamma_e} h_e\frac{\partial h^*}{\partial n}\mathrm{d}\Gamma + \sum_{i=1}^{n_b}\int_{\Gamma_{f(i)}} h_f\frac{\partial h^*}{\partial n}\mathrm{d}\Gamma =$$
$$-\frac{1}{K}\int_{\Gamma_e} h^* q_n \mathrm{d}\Gamma - \frac{1}{K}\sum_{i=1}^{n_b}\int_{\Gamma_{f(i)}} h^* q_f \mathrm{d}\Gamma \tag{11}$$

where: P^* is in Γ_e or in $\Gamma_f(i)$; h_e and h_f are hydraulic heads in Γ_e and $\Gamma_f(i)$, respectively; $q_n=-K(\partial h/\partial n)$ is the component of q along the outward normal of Γ_e. Note that when P^* is on $\Gamma_f(i)$, the integration is done on both on $\Gamma_t(i)$ and $\Gamma_b(i)$, so twice on the same elements and twice for the same collocation node, thus $c(P^*)$ is equal to 1.

The application of the approach entails the discretisation of the boundary into equal-length constant elements, marked by centroids. For simplicity and clarity of exposition, the numerical development of Equation 11 that follows is limited to the case of a single isolated fracture. Such a development can be easily extended to a network of fractures, through the application of Equation 6 for intersecting branches and the Dirichlet condition for branches intersecting the external boundaries, as described later. If N_e and N_f are the discretised elements of Γ_e and Γ_f (for simplicity Γ_f instead of $\Gamma_f(1)$ in what follows) respectively, there are N_e nodal quantities h_j and q_{nj} (j=1,...,N_e) on the block periphery, each couple associated to element Γ_{ej} of Γ_e, and N_f nodal quantities h_k and q_{fk} (with k=N_e+1,...,N_e+N_f) on the fractures, each couple associated to the element Γ_{fk} of Γ_f, and there are a total number of N_t=N_e+N_f nodes. By locating P^* in each centroid of Γ_e and Γ_f and by using the approximation in constant elements, Equation 11 for one isolated fracture can be written as follows:

$$c_i h_i + \sum_{j=1}^{N_\mathrm{e}} h_j \int_{\Gamma_{\mathrm{e}j}} \frac{\partial h^*}{\partial n}\mathrm{d}\Gamma + \sum_{k=N_\mathrm{e}+1}^{N_\mathrm{t}} h_k \int_{\Gamma_{\mathrm{f}k}} \frac{\partial h^*}{\partial n}\mathrm{d}\Gamma = -\frac{1}{K}\sum_{j=1}^{N_\mathrm{e}} q_{nj}\int_{\Gamma_{\mathrm{e}j}} h^*\mathrm{d}\Gamma - \sum_{k=N_\mathrm{e}+1}^{N_\mathrm{t}} q_{\mathrm{f}k}\int_{\Gamma_{\mathrm{f}k}} h^*\mathrm{d}\Gamma \tag{12}$$

where P^* collocation point coincides with node i, i=1,...,N_t, and h^* is defined in Equation 9.

By distinguishing if i is in Γ_e or Γ_f, Equation 12 can be split in two equations:

$$\sum_{j=1}^{N_\mathrm{e}} A_{ij}^{\mathrm{ee}} h_j + \sum_{k=N_\mathrm{e}+1}^{N_\mathrm{t}} A_{ik}^{\mathrm{ef}} h_k + \frac{1}{K}\sum_{j=1}^{N_\mathrm{e}} B_{ij}^{\mathrm{ee}} q_{nj} + \frac{1}{K}\sum_{k=N_\mathrm{e}+1}^{N_\mathrm{t}} B_{ik}^{ef} q_{\mathrm{f}k} = 0 \tag{13}$$

for i=1,**...**,N_e, and:

$$\sum_{j=1}^{N_\mathrm{e}} A_{ij}^{\mathrm{fe}} h_j + \sum_{k=N_\mathrm{e}+1}^{N_t} A_{ik}^{\mathrm{ff}} h_k + \frac{1}{K}\sum_{j=1}^{N_\mathrm{e}} B_{ij}^{\mathrm{fe}} q_{nj} + \frac{1}{K}\sum_{k=N_\mathrm{e}+1}^{N_t} B_{ik}^{\mathrm{ff}} q_{\mathrm{f}k} = 0 \tag{14}$$

for i=N_e+1,**...**,N_t, where **A**, **B** are matrices of coefficients, in which the first letter of the subscript denotes the boundary of the collocation node and the second letter the boundary of integration. The values of **A**, **B** are obtained by solving numerically the corresponding integral (Brebbia and Dominguez, 1992). Equation 14 can be re-written in a more concise form:

$$\begin{bmatrix}\mathbf{A}^{\mathrm{ee}} & \mathbf{A}^{\mathrm{ef}}\\ \mathbf{A}^{\mathrm{fe}} & \mathbf{A}^{\mathrm{ff}}\end{bmatrix}\begin{Bmatrix}\mathbf{h}^{\mathrm{e}}\\ \mathbf{h}^{\mathrm{f}}\end{Bmatrix} + \frac{1}{K}\begin{bmatrix}\mathbf{B}^{\mathrm{ee}} & \mathbf{B}^{\mathrm{ef}}\\ \mathbf{B}^{\mathrm{fe}} & \mathbf{B}^{\mathrm{ff}}\end{bmatrix}\begin{Bmatrix}\mathbf{q}_\mathrm{n}\\ \mathbf{q}_\mathrm{f}\end{Bmatrix} = 0 \tag{15}$$

where $\mathbf{h}^\mathrm{e}$ contains the hydraulic heads of the boundary nodes and $\mathbf{h}^\mathrm{f}$ contains the hydraulic heads of the N_f nodes of the fracture. In Equation 15 $\mathbf{h}^\mathrm{e}$ is known, therefore the equation can be rearranged as follows:

$$\begin{bmatrix}\mathbf{A}^{\mathrm{ef}}\\ \mathbf{A}^{\mathrm{ff}}\end{bmatrix}\mathrm{h}^{\mathrm{f}} + \frac{1}{K}\begin{bmatrix}\mathbf{B}^{\mathrm{ee}} & \mathbf{B}^{\mathrm{ef}}\\ \mathbf{B}^{\mathrm{fe}} & \mathbf{B}^{\mathrm{ff}}\end{bmatrix}\begin{Bmatrix}\mathbf{q}_\mathrm{n}\\ \mathbf{q}_\mathrm{f}\end{Bmatrix} = \mathbf{C} \tag{16}$$

where **C** includes the products $-\mathbf{A}^{\mathrm{ee}}\mathbf{h}^{\mathrm{e}}$ and $-\mathbf{A}^{\mathrm{fe}}\mathbf{h}^{\mathrm{e}}$. There are N_e+2N_f nodal unknowns. However, Equation 16 only consists of N_e+N_f equations, N_f additional equations are needed to solve the system. As previously mentioned, these complementary equations come from the numerical handling through a FEM representation of Equation 5, as shown below.

The numerical solution of the hydraulic head h^f leads to an error term $\epsilon(\xi)$ in Equation 5, i.e. (h=h^f in what follows):

$$\epsilon(\xi) = T\frac{\mathrm{d}^a h}{\mathrm{d}\xi^2} + q_\mathrm{f} \tag{17}$$

By resorting to the Galerkin's method of weighted residual, the integral from 0 to ℓ of $\epsilon(\xi)$, weighted by a function $w(\xi)$, is forced to 0:

$$\int_0^\ell T\frac{\mathrm{d}^2 h}{\mathrm{d}\xi^2}w(\xi)\mathrm{d}\xi + \int_0^\ell q_\mathrm{f} w\,(\xi)\mathrm{d}\xi = 0 \tag{18}$$

The first integral of Equation 18 can be solved by parts, giving:

$$-T\int_0^\ell \frac{\mathrm{d}w}{\mathrm{d}\ell}\frac{\mathrm{d}h}{\mathrm{d}\xi}\mathrm{d}\xi + T\frac{\mathrm{d}h}{\mathrm{d}\xi}w\Big|_0^\ell + \int_0^\ell q_f w(\xi)\mathrm{d}\xi = 0 \tag{19}$$

With reference to Figure 1, for the FEM representation, the fracture is divided in N_f+1 elements, delimited by the N_f nodes from the BEM discretisation and two auxiliary nodes at the two extremities (marked as 0 and N_f+1, respectively); the approximated solution for h is:

$$h(\xi) = N_0 h_0 + N_0 h_1 + \cdots + N_{N_\mathrm{f}+1}h_{N_\mathrm{f}+1} \tag{20}$$

where N_i, i=0,...,N_f+1, are linear shape functions, associated with the N_f+2 nodes. Note that the representation of h using linear shape functions is not consistent with the representation of the same quantity in Equation (12) with constant BEM elements. In addition, while the BEM elements have equal length ℓ_e, equal to ℓ/N_f, the FEM elements delimited by the nodes 0 and 1, and by the nodes N_f and N_f+1 have length equal to $\ell_\mathrm{e}/2$, the remaining elements have length ℓ_e. Through the linear functions, the derivative of h in Equation (19) is better represented while the inconsistency of the representations of h should not lead to significant errors. The representation of q_f is instead constant per each element and consistent with the corresponding BEM representation.

By using the approximated solution of Equation (20) and (19) and by imposing w=N_i (i.e. the weighting function coincides with the shape function), N_f additional equations can be obtained:

$$-T\int_0^\ell \frac{\mathrm{d}N_i}{\mathrm{d}\xi}\frac{\mathrm{d}N_j}{\mathrm{d}\xi}h_j\mathrm{d}\xi + \int_0^\ell q_\mathrm{f} N_i\mathrm{d}\xi = 0 \tag{21}$$

for i=1,...,N_f, j=0,1,...,N_f+1. Note that the second term in Eq. 19 is removed because the derivative of h is nil at ξ=0 and ξ=ℓ, being the discharge Q at both the extremities of an isolated fracture also nil. Function N_i is defined in the elements astride node i only, thus in Equation (21) only the quantities h_{i-1}, h_i, h_{i+1}, and $q_{\mathrm{f},i-1}$, $q_{\mathrm{f},i}$, $q_{\mathrm{f},i+1}$ are included. By computing the integrals the following equation derives for node i=2,…,N_f –1 (see Figure 1):

$$\frac{T}{2\ell_e^2}(h_{i-1} - 2h_i + h_{i+1}) + \frac{1}{8}\left(q_{\mathrm{f},i-1} + 6q_{\mathrm{f},i} + q_{\mathrm{f},i+1}\right) = 0 \tag{22}$$

The equations for nodes 1 and N_f are somewhat different because the length of the most extreme elements is $\ell_\mathrm{e}/2$ and they contain h_0 and h_{N_f+1}, which are not unknowns, rather they can be related to the hydraulic heads of the proximal nodes by writing Equation (21) for i=0 and i=N_f+1. Note that in Equation (21) the discharge Q at the extremities is implicitly set to 0; one has:

$$h(\xi = 0) = h_0 = h_1 - \frac{q_{\mathrm{f},1}\ell_\mathrm{e}^2}{4T},$$
$$\tilde{h}(\xi = \ell) = \tilde{h}_{N_f+1} = h_{N_\mathrm{f}} + \frac{q_{\mathrm{f},N_\mathrm{f}}\ell_\mathrm{e}^2}{4T} \tag{23}$$

Equation 22 for nodes i=2,…,N_f –1 and the special equation for nodes 1 and N_f can be grouped as follows:

$$T\mathbf{a}\mathbf{h}^\mathrm{f} + \mathbf{b}\mathbf{q}_\mathrm{f} = 0 \tag{24}$$

where $\boldsymbol{h}^\mathrm{f}$ refers to the hydraulic head of fracture nodes and **a**, **b** are matrices of coefficients.

Equations (16) and (24) constitute the global set of algebraic equations required to solve the steady-state fluid flow in a rectangular block with a single isolated fracture under the boundary conditions described in the previous section to impose the directional hydraulic gradients and with q_f representing the coupling quantities.

For the extension to a network of fractures, Equation (24) is written for each branch of the network by implementing the volumetric budget at the intersections among fractures. Given an intersection I with $n_{\mathrm{ib}}(I)$ (3 or 4) intersecting fracture branches, Equation 6 is applied in conjunction with Equation (21) written for each branch i. Note that in this case, in Equation (21) the second term of Equation (19) is preserved, including the discharge Q_i at the branch extremity coinciding with intersection I. By managing the equations, an expression containing the hydraulic head at the intersection, the hydraulic heads and the normal components of the specific discharge at the proximate nodes of the fracture branches derives. This expression is easily incorporated in the equations for all the fracture branches to remove the hydraulic head at the intersection. Finally, for a branch extremity at the block boundary, the Dirichlet condition applied to the intersected edge of the block is directly included in Equation (24) for that branch, instead of using Equation (23).

Boundary conditions different from the ones previously described (i.e. prescribed normal components of the discharge at the boundary, fixed values of the discharge at the extremities of the branches intersecting the boundaries) can be applied by slightly modifying the previous equations. However, the examples reported below do not refer to the application of such boundary conditions. The approach and the dedicated code are designed for the assessment of the hydraulic conductivity, thus only simulations with imposed directional hydraulic gradients are considered.

3 NUMERICAL VALIDATIONS

3.1 Numerical validations

The first validation example refers to the scheme in Figure 3a, consisting of a 1×1 m^2 porous block with the hydraulic conductivity K of 1.0×10^{-5} ms^{-1} and a 0.80 m-long slanted fracture, having the transmissivity T of 1.0×10^{-4} m^{2}s^{-1}, passing through the centre of the block and inclined at angle θ with respect to the horizontal axis x (in Figure 3a θ is 30°). Given the boundary conditions on the edges, a directional hydraulic gradient J_y along y equal to 1m/m is applied ($J_y=-\partial h/\partial y$). For θ equal to 0º, 15º, 30º, 45º, 60º, 75º, 90°, the discharges Q_t, crossing the top edge, and Q_r, crossing the right vertical edge are computed by using the proposed approach and compared to the results produced with COMSOL Multiphysics (FEM) simulations. For this validation example, the discretisation used consists of only 10 BEM elements on each single block edge and 4 BEM/FEM elements on the fracture; for the FEM simulation, the number of quadratic elements used and nodes (depending on the fracture orientation) are instead more than 5500 and almost 11500, respectively, see mesh example shown in Figure 3b (also here θ is 30°). Despite the coarse mesh utilised in the example, the maximum difference between the two sets of results is only 5%. The reason for such a difference may be due to the more refined FEM representation, especially around the extremities of the fracture. However, it is worthwhile to mention that a perfect match between the two solutions cannot be obtained because in the proposed approach the gradients along the fracture at its extremities are null, which are different in the FEM solution.

Note that the values of hydraulic head in inner points P of the domain are not part of the solution and can be obtained for any point by using Equation 11 with the collocation point P^* coinciding with P and once all the values of h and q_f are retrieved from the final solution. Again, the integrals in Equation 11 are numerically solved. The specific discharge components can be instead obtained by differentiating by x or y the same equation (Equation 11), with the integrals of these new equations still to be solved numerically. However, these estimations are not necessary in this case, given that the objective is the computation of the discharges exiting/entering the block, so these computations are not implemented in the published code.

The second validation example refers to the scheme shown in Figure 5. An orthogonal fracture network is embedded into a 1×1m^2 porous block (K=1.0×10^{-7}ms^{-1}) with random fracture spacing. The transmissivity T is the same for all fractures and is equal to 1.0×10^{-5}m^{2}s^{-1}. The boundary conditions are such to induce a global directional hydraulic gradient equal to 1 along y (same as in the scheme of Figure 1). For Q_t the following closed-form solution is available; Q_t=K+5T, thus Q_t=5.0×10^{-5}m^{2}s^{-1}. The discharge Q_r is zero. By using only 6 equal-length constant boundary elements for the block edges and 4 equal-length constant boundary elements for the fracture edges, the numerical results are practically the same, while Q_r is only 0.5×10^{-8}m^{2}s^{-1}, despite the discretisation of the edges is performed independently of the location of the intersections of the fractures with the edges. This example demonstrates the quality of the FEM representation for the fracture discharge. In addition, it is apparent that the numerical scheme is well modelled, as the values of all unknown quantities obtained are as expected, including the q_f values (all nil).

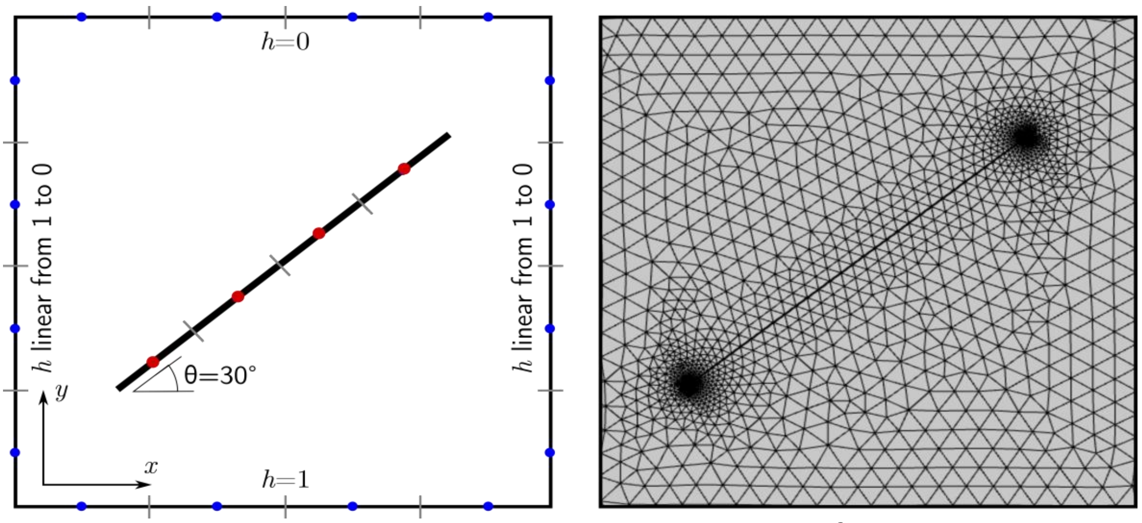

Fig. 3. Discretisation for the solution of the fluid flow driven by a directional gradient J_y in a 1x1m^2 block of a porous medium and a slanted isolated transmissive fracture: a) proposed approach: blue dots - BEM nodes on the block edges, red dots - BEM/FEM nodes on the fracture; b) COMSOL Multiphysics FEM mesh.

To further demonstrate the quality of the solution when an exchange between fractures and matrix occurs, an additional simulation is performed for the same scheme with a modified transmissivity T of 1.0×10^{-9}m^{2}s^{-1} ascribed to the branches marked blue in Fig. 5. The new value of Q_t is 2.1×10^{-5}m^{2}s^{-1}.

Fig. 6 shows the q_f distributions along fractures A-B (branches numbers 49 to 54) and C–D (branches numbers 55 to 60). It is apparent that due to the "barrier" constituted by the fracture branches with reduced transmissivities the flow is diverted towards the more conductive zones of the domain, with the fractures A-B and C-D storing fluid from the porous matrix (positive q_f values) and releasing it at the right vertical boundary and (less) to the matrix (negative q_f values).

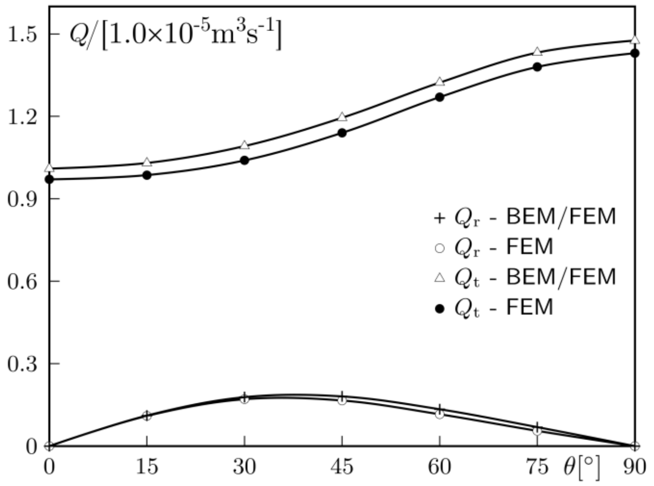

Fig. 4. Comparison of the results obtained from the proposed method (BEM/FEM) and the results from COMSOL Multiphysics (FEM) with reference to the scheme of Figure 3, a porous block with a slanted fracture, subjected to a vertical hydraulic gradient of 1m/m directed upward; Q_r discharge on the right edge, Q_t discharge on the top edge.

The third validation example as shown in Figure 7 is sourced from Priest (1993), where a 10×10m^2 square is dissected by a fracture network. Note the node coordinates of the fracture networks may slightly differ from the original values. The fracture transmissivity T in m^{2}s^{-1} is obtained from the conductivity C values (given in Table 11.3 of Priest, 1993) divided by the corresponding "channel" length. To ensure an "impervious" matrix material, the block hydraulic conductivity K is set to a small value of 1.0×10^{-10} ms^{-1}. In Table 1 the coordinates (x_1,y_1) and (x_2,y_2) of the extremities of the 21 fracture branches and their corresponding T values in m^{2}s^{-1} are listed. The boundary conditions are defined by the hydraulic head h, which, by default settings of the code, is equal to 1 m on the left vertical boundary, 0 m on the right vertical boundary, linear from 1 to 0 m on the other two boundaries.

For the simulation, a rough BEM mesh is used, consisting of 6 BEM constant elements on the block boundaries and 4 on each fracture branch. In Table 2, for each fracture intersection node, the values of the hydraulic head of the most proximate BEM nodes (the values exactly at the intersection points are not available from the code by the numerical implementation) are given, and their relative average values h_m are reported.

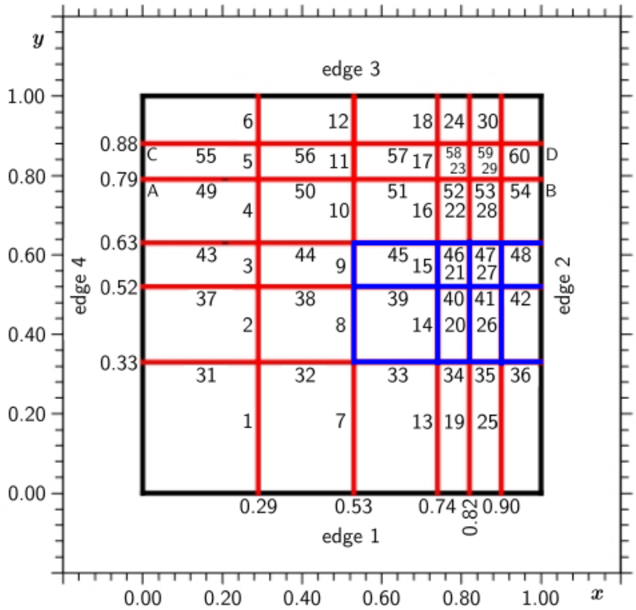

Fig. 5. Scheme of the second validation example; fractures of the orthogonal network (blue and red lines) are subdivided in branches, numbered from 1 to 60, with blue branches having reduced transmissivity in the additional simulation (x,y in m).

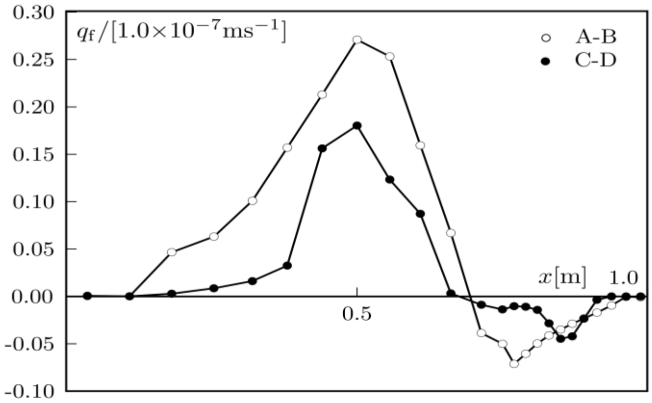

Fig. 6. Distribution of q_f fracture discharges along lines A-B and C-D of the scheme shown in Figure 5 (second validation example).

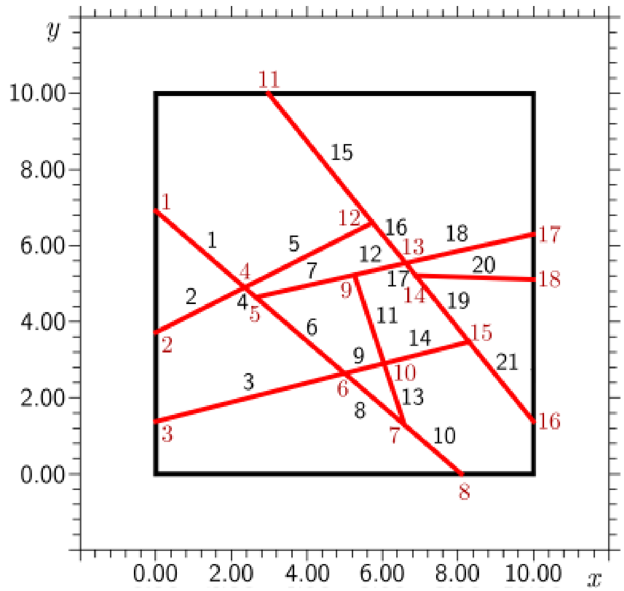

Fig. 7. Scheme of the third validation example; node numbers are in red and branch numbers are in black.

For the comparison with the values from Priest (1993), note that in the original example the h boundary values of the hydraulic head at the left vertical and right vertical boundaries are 3 and 1 m, respectively, therefore, given that the boundary conditions are proportional, the values h_P from Priest are scaled to obtain the h_{Ps} values, that are compared with the average values h_m provided by the code. The comparison is very encouraging, showing again the good modelling capability of the numerical scheme in the proposed method. This validation sets the foundation for the application example described below.

Table 1. Coordinates (x_1, y_1),(x_2, y_2) [m] of the extremities of the 21 fracture branches and the corresponding T values [m^{2}s^{-1}] for the third validation example.

branch#	x_1	y_1	x_2	y_2	T
1	0.000	6.910	2.350	4.900	0.3034E–06
2	0.000	3.720	2.350	4.900	0.3824E–05
3	0.000	1.380	5.000	2.640	0.1099E–04
4	2.350	4.900	2.650	4.640	0.1314E–06
5	2.350	4.900	5.740	6.600	0.3214E–05
6	2.650	4.640	5.000	2.640	0.2653E–06
7	2.650	4.640	5.260	5.230	0.5103E–05
8	5.000	2.640	6.590	1.280	0.3016E–06
9	5.000	2.640	6.040	2.900	0.1275E–04
10	6.590	1.280	8.090	0.000	0.3067E–06
11	5.260	5.230	6.040	2.900	0.5143E–06
12	5.260	5.230	6.620	5.540	0.4582E–05
13	6.040	2.900	6.590	1.280	0.6376E–06
14	6.040	2.900	8.290	3.470	0.1028E–04
15	2.980	10.00	5.740	6.600	0.1798E–06
16	5.740	6.600	6.620	5.540	0.1934E–06
17	6.620	5.540	6.880	5.210	0.5684E–07
18	6.620	5.540	10.00	6.300	0.4524E–05
19	6.880	5.210	8.290	3.470	0.1973E–06
20	6.880	5.210	10.00	5.110	0.2076E–05
21	8.290	3.470	10.00	1.380	0.2158E–06

Table 2. Hydraulic head h values at the intersections from the simulation and comparison with the corresponding values from Priest (1993); h_i are values at the proximate BEM nodes, as obtained directly from codes, h_m average values, h_P values from Priest (1993), and h_{Ps} scaled h_P values in consideration of the boundary conditions of Priest (1993).

n#	h_1	h_2	h_3	h_4	h_m	h_P	h_{Ps}
4	0.878	0.877	0.807	0.849	0.853	2.720	0.860
5	0.485	0.420	0.483	–	0.463	1.863	0.432
6	0.863	0.822	0.840	0.792	0.829	2.687	0.844
7	0.700	0.618	0.697	–	0.672	2.362	0.681
9	0.351	0.328	0.399	–	0.359	1.677	0.339
10	0.822	0.759	0.816	0.802	0.800	2.640	0.820
12	0.782	0.762	0.706	–	0.750	2.541	0.771
13	0.264	0.237	0.319	0.225	0.261	1.508	0.254
14	0.134	0.201	0.102	–	0.146	1.235	0.118
15	0.795	0.708	0.693	–	0.732	2.585	0.793

4 APPLICATION EXAMPLE

As previously mentioned, a straight application of the proposed approach is the quantification of the tensor of equivalent conductivity $\mathbf{K}^e$ of a porous block with embedded fractures. For such a quantification, a directional gradient induced by specific boundary conditions is applied to the blocks and the corresponding discharges at the boundaries of the blocks are computed and used to derive the components of the hydraulic conductivity tensor. The boundary conditions are as the ones shown in Figure 2. If D is the size of the block, the hydraulic head at the bottom is 1, 0 on the opposite edge and linear along the other two edges, then the hydraulic gradient is $1/D$ and is directed along y^+. Being Q_t the global discharge at the top boundary, then K^e_{yy} is equal to Q_t. If Q_r is the discharge through the right boundary, then K^e_{yx} is equal to Q_r. To derive the other two components of $\mathbf{K^e}$, namely K^e_{xx} and K^e_{xy} it is sufficient to orient the hydraulic gradient along x^+ by imposing the hydraulic head of 1 on the left vertical boundary, and 0 on the opposite boundary and linear along the other two boundaries. A check of the obtained values can be performed by computing the discharge by orienting the gradient along y^- and x^-.

Table 3. Results of the sensitivity analysis for the application example; K (variable) hydraulic conductivity of the rock matrix, K^e_{xx}, K^e_{xy}, K^e_{yx}, K^e_{yy} components of the K^e equivalent hydraulic tensor (conductivities in ms^{-1}).

K	K^e_{xx}	K^e_{xy}	K^e_{yx}	K^e_{yy}	K^e_{xx}/K^e_{yy}	$[(K^e_{xx}+K^e_{yy})/2]/K$
1.0×10^{-8}	0.509×10^{-6}	0.421×10^{-8}	0.140×10^{-6}	0.338×10^{-7}	15.06	27.14
5.0×10^{-8}	0.632×10^{-6}	0.796×10^{-8}	0.137×10^{-6}	0.796×10^{-7}	7.94	7.12
1.0×10^{-7}	0.755×10^{-6}	0.107×10^{-7}	0.131×10^{-6}	0.135×10^{-6}	5.59	4.45
5.0×10^{-7}	0.139×10^{-5}	0.201×10^{-7}	0.108×10^{-6}	0.567×10^{-6}	2.45	1.96
1.0×10^{-6}	0.199×10^{-5}	0.252×10^{-7}	0.107×10^{-6}	0.109×10^{-5}	1.83	1.54
5.0×10^{-6}	0.627×10^{-5}	0.240×10^{-7}	0.179×10^{-6}	0.524×10^{-5}	1.20	1.15
1.0×10^{-5}	0.115×10^{-4}	0.162×10^{-7}	0.225×10^{-6}	0.104×10^{-4}	1.11	1.10
5.0×10^{-5}	0.530×10^{-4}	0.769×10^{-7}	0.299×10^{-6}	0.519×10^{-4}	1.02	1.05
1.0×10^{-4}	0.104×10^{-3}	0.178×10^{-8}	0.312×10^{-6}	0.103×10^{-3}	1.01	1.04

To illustrate the quantification of $\mathbf{K^e}$ and demonstrate the quality of the proposed approach, the third validation example is further analysed with a matrix hydraulic conductivity K changing from $1.0\times10^{-8}ms^{-1}$ to $1.0\times10^{-4}ms^{-1}$. The values of K^e_{xx}, K^e_{xy}, K^e_{yx}, and K^e_{yy} are listed in Table 3 for each simulation, together with the values of K^e_{xx}/K^e_{yy} and $[(K^e_{xx}+K^e_{yy})/2]/K$, where the first ratio is an indication of the anisotropy of the tensor and the second one refers to the relative importance of the DFN in conveying fluid with respect to the matrix. The variations of K^e_{xx}/K^e_{yy} and $[(K^e_{xx}+K^e_{yy})/2]/K$ as K increases are also shown in Figure 8. It is apparent from the results, as expected, that the tensor tends to more isotropic with increasing K, the ratio of K^e_{xx}/K^e_{yy} gets closer to 1 and the equivalent conductivity is less affected by the DFN (the average conductivity becomes closer to the matrix conductivity, i.e. $[(K^e_{xx}+K^e_{yy})/2]/K$ becomes closer to 1).

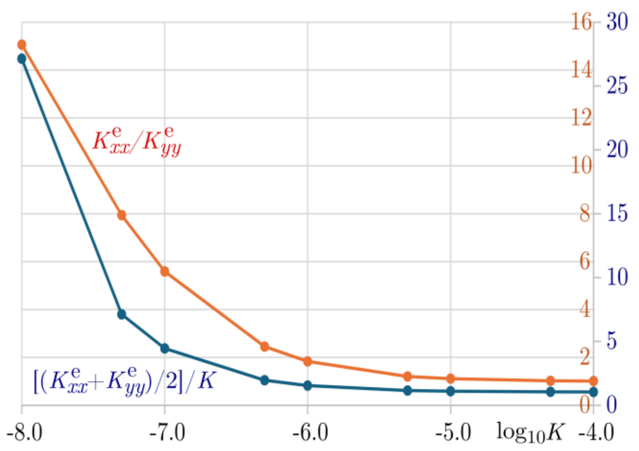

Fig. 8. Application example: variations of K^e_{xx}/K^e_{yy} and $[(K^e_{xx}+K^e_{yy})/2]/K$ versus $\log_{10}K$.

However, it is worthwhile to mention that, even for high values of K, K^e_{xy} substantially differs from K^e_{yx}, although both values are more marginal with respect to K^e_{xx} and K^e_{yy}, and the tensor is not symmetric. This feature is common in fractured porous medium, particularly when there are relatively few fractures regardless of the transmissivity. Note also for low K values, one order of magnitude difference between K^e_{xx} and K^e_{xy} is due to the dominant directionality of the fracture network in x direction. This application analysis again demonstrates the capability of the proposed method to evaluate the equivalent hydraulic conductivity tensor in fractured porous media.

5 CONCLUSION

In this paper, a numerical modelling approach based on coupling BEM with FEM is presented for the solution of 2D steady-state fluid flow in fractured porous rocks, with particular focus on the estimation of the conductivity tensor of an equivalent porous medium. The rock matrix is considered a homogeneous isotropic porous material, whereas fractures are zero-width linear elements of given transmissivities. BEM is applied to the porous rock matrix, while the flow in the fractures is handled by resorting to linear FEM discretisation. The coupling terms between matrix and fractures are the discharge components normal to fractures at the contact points. The approach is reliant on constant BEM elements to handle the flux discontinuities occurring at fracture-fracture and fracture-boundary intersections. Examples are provided to demonstrate that, despite the rough approximation given by constant BEM elements and linear FEM elements, satisfactory results are obtained.

Both fractures and block boundaries are discretised by using equal-size elements, thus the pre-processing is fast with no special prescriptions. It is worthwhile noting that the geometry of fracture networks in rock masses is in general not deterministic, therefore it is not necessary to pursue a highly sophisticated numerical solution for validation purposes. In practice, normally multiple realisations of the fracture network may be necessary in the context of a Monte Carlo process. The proposed method expedites the computation to recover key hydraulic features of the fractured porous rock mass.

Acknowledgements. The authors would like to acknowledge the National Research Council of Italy (CNR) for the funding provided in the context of the CNR Short Term Mobility Programme.

REFERENCES

Barenblatt, G.I., Zheltov, Yu.P., Kochina, I.N.,1960. Prikl. Mat. Mekh, 24, 5, 1286–1303.

Bear, J., Cheng, A.H.D., 2010. Modelling groundwater flow and contaminant transport. Springer, 834p.

Benke, R., Painter, S., 2003. Modeling conservative tracer transport in fracture networks with a hybrid approach based on the Boltzmann transport equation. Water Resour. Res., 39, 11, 1324.

Berrone, S., Borio, A., Fidelibus, C., Pieraccini, S., Scialò, S., Vicini, F., 2018. Advanced computation of steady-state fluid flow in discrete fracture-matrix models: FEM-BEM and VEM-VEM fracture-block coupling. GEM Int. J. Geomath., 9, 2, 377–399.

Brebbia, C.A., Dominguez, J., 1992. Boundary Elements: An Introductory Course. WIT Press, Southampton, UK.

Březina, J., Stebel, J., 2016. Analysis of Model Error for a Continuum-Fracture Model of Porous Media Flow. In: Kozubek, T., Blaheta, R., Šístek, J., Rozložník, M., Čermák, M. (eds), High Performance Computing in Science and Engineering 2015. Lecture Notes in Computer Science, vol 9611, Springer, Cham.

Bruel, D., 2007. Using the migration of the induced seismicity as a constraint for fractured hot dry rock reservoir modelling. Int. J. Rock Mech. Min. Sci., 44, 1106–1117.

Cacas, M.C., Ledoux, E., de Marsily, G., Barbreau, A., Calmels, P., Gaillard, B., Margrita, R., 1990. Modelling fracture flow with a stochastic discrete fracture network: calibration and validation - the transport model. Water Resour. Res., 26, 3, 491–500.

Cacas, M.C., Ledoux, E., de Marsily, G., Tillie, B., Barbreau, A., Durand, E., Feuga, B., Paudecerf, P., 1990. Modeling fracture flow with a stochastic discrete fracture network: calibration and validation: 1. The flow model. Water Resour. Res., 26, 3, 479–489.

Chen, Z., Liao, X., Sepehrnoori, K., Yu, W., 2018. A semianalytical model for pressure-transient analysis of fractured wells in unconventional plays with arbitrarily distributed discrete fractures. Soc. Pet. Eng. J., 23, 2041–2059.

COMSOL AB, 2024. COMSOL Multiphysics® v. 6.3, Stockholm, Sweden.

de Dreuzy, J.R., Davy, P., Bour, O., 2001. Hydraulic properties of two dimensional random networks following a power law length distribution: 1. Effective connectivity. Water Resour. Res., 37, 8, 2065–2078.

Dershowitz, W.S., Einstein, H.H., 1988. Characterizing rock joint geometry with joint system models. Rock Mech. Rock. Eng., 21, 21–51.

Dershowitz, W.S., Fidelibus, C., 1999. Derivation of equivalent pipe network analogues for three-dimensional discrete fracture networks by boundary element method. Water Resour. Res., 35, 9, 2685–2691.

Huang, N., Jiang, Y., Liu, R., Li, B., 2017. Estimation of permeability of 3-D discrete fracture networks: an alternative possibility based on trace map analysis. Eng. Geol., 226, 12–19.

Hyman, J.D., Dentz, M., Hagberg, A., Kang, P.K., 2019. Linking structural and transport properties in three-dimensional fracture networks. J. Geophys. Res. Solid Earth, 124, 1185–2104.

Kang, P., Le Borgne, T., Dentz, M., Bour, O., Juanes, R., 2015. Impact of velocity correlation and distribution on transport in fractured media: field evidence and theoretical model. Water Resour. Res., 51, 940–959.

Lee, S.H., Lough, M.F., Jensen, C.L., 2001. Hierarchical modelling of flow in naturally fractured formations with multiple length scales. Water Resour. Res., 37, 3, 443–355.

Lenti, V., Fidelibus, C., 2003. A BEM solution of steady-state flow problems in discrete fracture networks with minimization of core storage. Comput. Geosci., 29, 9, 1183–1190.

Li, P., Schanz, M., 2013. Time domain boundary element formulation for partially saturated poroelasticity. Eng. Anal. Bound. Elem., 37, 11, 1483–1498.

Long, J.C.S., Remer, J.S., Wilson, C.R., Witherspoon, P.A., 1982. Porous media equivalents for networks of discontinuous fractures. Water Resour. Res., 18, 3, 645–658.

Lough, M.F., Lee, S.H., Kamath, J., 1998. An efficient boundary integral formulation for flow through fractured porous media. J. Comput. Phys., 143, 462–483.

Martin, V., Jaffré, J., Roberts, J.E., 2005. Modeling fractures and barriers as interfaces for flow in porous media, SIAM J. Sci. Comput., 26, 1667–1691.

Neuman, S.P., 2005. Trends, prospects and challenges in quantifying flow and transport through fractured rocks. Hydrogeol. J., 13, 124–147.

Nieber, J.L., Sidle, R.C., 2010. How do disconnected macropores in sloping soils facilitate preferential flow? Hydrol. Process. 24, 1582–1594.

Pan, J.B., Lee, C.C., Lee, C.H., Yeh, H.F., Lin, H.I., 2010. Application of fracture network model with crack permeability tensor on flow and transport in fractured rock. Eng. Geol., 116, 166–177.

Pichot, G., Erhel, J., De Dreuzy, J., 2012. A generalized mixed hybrid mortar method for solving flow in stochastic discrete fracture networks. SIAM J. Sci. Comput., 34, 1, B86–B105.

Priest, S.D., 1993. Discontinuity Analysis for Rock Engineering. Chapman and Hall, London

Pruess, K., Narasimhan, T., 1985. Practical method for modelling fluid and heat flow in porous media. Soc. Pet. Eng. J., 25, 14–26.

Rasmussen, T.C., 1991. Steady fluid flow and travel times in partially saturated fractures using a discrete air-water interface. Water Resour. Res., 27, 1, 67–76.

Rasmussen, T.C., Yeh, T.C.J., Evans, D.D., 1989. Effect of variable fracture permeability/matrix permeability ratios on three-dimensional fractured rock hydraulic conductivity. Battelle Columbus Division, OH, pp. 337–358.

Reeves, D.M., Parashar, R., Pohlmann, K., Russell, C., Chapman, J., 2014. Development and calibration of dual-permeability models with discontinuous fault networks. Vadose Zone J., 13, 8.

Reichenberger, V., Jakobs, H., Bastian, P., Helmig, R., 2006. A mixed-dimensional finite volume method for two-phase flow in fractured porous media, Adv. Water Resour., 29, 1020–1036.

Ren, F., Ma, G., Fan, L., Wang, Y., Zhu, H., 2017. Equivalent discrete fracture networks for modelling fluid flow in highly fractured rock mass. Eng. Geol., 229, 21–30.

Renshaw, C.E., 1999. Connectivity of joint networks with power law length distributions. Water Resour. Res., 35, 9, 2661–2670.

Ronayne, M.J., Gorelick, S.M., 2006. Effective permeability of porous media containing branching channel networks. Phys. Rev. E, 73, 026305.

Samardzioska, T., Popov, V., 2005. Numerical comparison of the equivalent continuum, non-homogeneous and dual porosity models for flow and transport in fractured porous media. Adv. Water Resour., 28, 235–255.

Sandve T.H., Berre I., Nordbotten, J.M., 2012. An efficient multi-point flux approximation method for discrete fracture–matrix simulations. J. Comput. Phys., 231, 3784–3800.

Shapiro, A. M., Andersson, J., 1983. Steady state fluid response in fractured rock: A boundary element solution for a coupled, discrete fracture continuum model. Water Resour. Res., 19, 4, 959–969.

Shapiro, A.M., Andersson, J., 1985. Simulation of steady-state flow in three-dimensional fracture networks using the boundary element method. Adv. Water Resour., 8, 3, 106–110.

Therrien, R., Sudicky, E.A., 1996. Three-dimensional analysis of variably-saturated flow and solute transport in discretely-fractured porous media. J. Contam. Hydrol., 23, 1–44.

Wang, B., Feng, Y., Zhou, X., Pieraccini, S., Scialò, S., Fidelibus, C., 2022. Discontinuous boundary elements for steady-state fluid flow problems in discrete fracture networks. Adv. Water Resour., 161, 104125.

Xu, C., Dowd, P.A., 2014. Stochastic fracture propagation modelling for enhanced geothermal systems. Math. Geosci., 46, 665–690.

Xu, C., Dowd, P.A., Nguyen, N., Wang, W. J., 2020. Non-parametric three-dimensional fracture modelling from fracture mapping data, in special issue: “Statistical analysis and modelling of fractures and fracture networks in rock masses” of Boletín Geológico y Minero , 131 (3): 401–422.

Xu, C., Dowd, P.A., Wyborn, D., 2013. Optimisation of a stochastic rock fracture model using Markov Chain Monte Carlo simulation. Min. Tech. Trans. Inst. Min. Metall. A, 122, 3, 153–158.

Xu, C., Fidelibus, C., Dowd, P., Wang, Z., Tian, Z., 2018. An iterative procedure for the simulation of the steady-state fluid flow in rock fracture networks. Eng. Geol., 242, 160–168.

Xu, C., Fidelibus, C., Dowd, P.A., 2014. Realistic pipe models for flow modelling in discrete fracture networks. Proceedings of DFNE2014, Vancouver, Canada.

Yang, R., Huang, Z., Yu, W., Li, G., Ren, W., Zuo, L., Tan, X., Sepehrnoori, K., Tian, S., Sheng, M., 2016. A comprehensive model for real gas transport in shale formations with complex non-planar fracture networks. Sci. Rep., 6, 36673.

Received 02 April 2024
Accepted 24 January 2025